Mon. Not. R. astr. Soc. (1983) **202**, 881–901

Normal modes of Bardeen discs – II. A sequence of $n = 2$ polytropes

Bernard F. Schutz and Enric Verdaguer* *Department of Applied Mathematics and Astronomy, University College, PO Box 78, Cardiff CF1 1XL*

Received 1982 May 6; in original form 1981 March 3

Summary. We study in detail the normal modes of a sequence of differentially rotating, inviscid polytropic fluid discs in the Bardeen approximation. The equilibrium isentropic self-gravitating discs have comparable pressure and rotational support. At the low-angular-momentum end of the sequence, discs are secularly and dynamically stable; at the high end they possess two dynamically and two extra secularly unstable modes. We identify two types of modes, called p- and r-modes, for which we introduce a classification scheme based upon a number of criteria, including winding numbers in phase diagrams. Most of the r-modes have corotation points and seem to be finite-dimensional approximations to a continuous spectrum, caused by differential rotation, but we also observe p-modes with corotation points which seem to remain discrete modes even inside the continuous spectrum. In fact, dynamical instability sets in through such modes, in a disc in which the ratio τ of kinetic to potential energy is 0.27. Secular instability to gravitational radiation sets in via a zero-frequency p-mode when $\tau = 0.1221$. The r-modes are never unstable. Apart from obvious effects of differential rotation, the qualitative behaviour of eigenfrequencies along this sequence bears a striking resemblance to that along the Maclaurin sequence of incompressible fluids. In an appendix we describe an inexpensive test of the numerical accuracy of eigenfrequencies.

1 Introduction

This is the second paper in a series which studies the normal modes of Bardeen discs in order to gain insight into the general problem of the stability and normal modes of differentially rotating highly oblate stars. Our motivation for studying these discs was explained in the first paper in the series, Schutz & Bowen (1983, Paper I), which studied the simplest discs analytically. In this paper we study a sequence of discs with polytropic index $n = 2$ and considerable differential rotation. We find a whole range of complicated and interesting behaviour of the eigenfrequencies along the sequence: the apparent existence of a

* On leave from Universitat Autonoma de Barcelona, Spain.

continuous spectrum dominated by Rossby-type modes; the passage of low-order Rossby modes from the discrete spectrum into the continuous one as the differential rotation increases; the presence of low-order p-type discrete-frequency modes in the middle of the continuous spectrum in the more rapidly rotating discs; the onset of dynamical instability in the fundamental bar mode at a point where its frequency is inside the continuous spectrum; and the onset of the gravitational-radiation secular instability for the bar mode through a zero-frequency mode. We discuss the classification of modes and propose a nomenclature for them. We also investigate the possibility of using phase diagrams to classify modes, as is done for non-rotating stars. A more detailed investigation of the continuous spectrum and analytic calculations aimed at understanding these modes will be presented in a subsequent paper (Verdaguer 1983). For references to related work on polytropic discs, see Paper I.

2 Setting up the problem

The construction of the unperturbed discs and the equations governing their perturbations are described by Bardeen (1975). The idea is to calculate the stucture of a highly oblate rotating polytrope only to first order in its polar thickness. This reduces the equilibrium equation from two dimensions down to one. In cylindrical coordinates (r, ϕ, z) and for an $n = 2$ polytrope whose equation of state is

$$p = K\rho^{3/2}, \tag{1}$$

the equilibrium equation is

$$\Omega^2 r = -\frac{d}{dr}[\nu_c - \kappa\sigma^{2/3}], \tag{2}$$

where σ is the surface density of the disc (integral of its volume density ρ over z), Ω is its angular velocity, ν_c is the gravitational potential produced by an *infinitesimally thin* disc, (a 'cold' disc) of the same surface density,

$$\nabla^2\nu_c = 4\pi G\sigma(r)\,\delta(z), \tag{3}$$

and κ is a parameter which governs the polar thickness of the disc. The final term in (2) is an effective potential which combines two effects: the contribution of pressure and the weakening of the gravitational field relative to ν_c because the mass is not all concentrated in the plane $z = 0$. Both effects depend linearly on the parameter κ, defined as

$$\kappa = (\tfrac{1}{2}\pi G K^2)^{1/3} B(\tfrac{1}{2}, 1/3), \tag{4}$$

where $B(n, m)$ is the beta function and K parametrizes the polytropic equation of state (1). Clearly, this measures the 'warmth' of the disc, and our numerical sequence of discs is constructed by varying κ while keeping $\sigma(r)$ fixed. Fig. 1 shows this universal surface density. For displaying our results, however, we shall replace κ by the more usual parameter τ, the ratio of kinetic to potential energy of the equilibrium disc, which is found by numerical integration.

Perturbations of these discs may be treated under similar approximations as for the equilibrium structure, with the added assumption that equilibrium is always maintained in the z-direction. The Eulerian perturbations $\delta\sigma$, $\delta\Omega$, and δv (radial velocity) are in fact z-averages of the true perturbations. If we look for a normal mode of frequency ω and axial

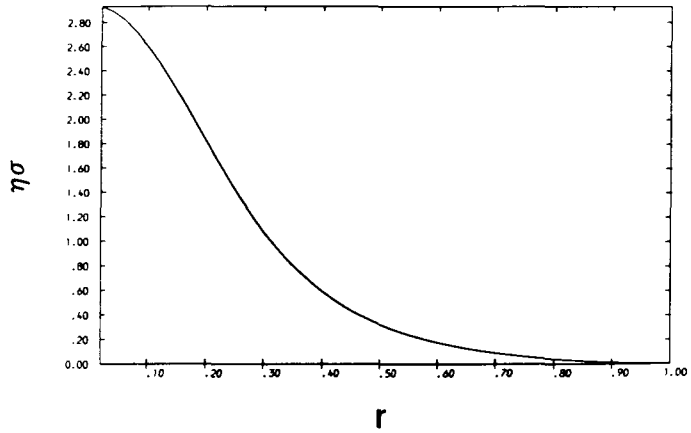

Figure 1. The surface density of the unperturbed discs. All discs in the sequence have this density. Units are chosen so that the mass and radius of the discs equal unity.

eigenvalue m (i.e. scalar perturbations proportional to $\exp(i\omega t + im\phi)$), we need to solve the ordinary differential equations

$$(\omega + m\Omega)\delta\sigma - i\frac{1}{r}\frac{d}{dr}(\sigma r\delta v) + m\sigma\delta\Omega = 0, \tag{5}$$

$$i\frac{d}{dr}\delta(v_c - \kappa\sigma^{2/3}) + (\omega + m\Omega)\delta v + 2ir\Omega\delta\Omega = 0, \tag{6}$$

$$-m\frac{1}{r^2}\delta(v_c - \kappa\sigma^{2/3}) - i\frac{1}{r^2}\frac{d}{dr}(r^2\Omega)\delta v + (\omega + m\Omega)\delta\Omega = 0. \tag{7}$$

Because we are dealing with polytropes, the solutions can be scaled. Results in this paper are chosen in units in which the mass M and radius R of the discs equal 1 and the angular velocity at the rim of the *cold* disc ($\kappa = 0$) equals 1. The angular velocities of several warm discs in our sequence are displayed in these units in Fig. 2.

Solutions of (5)–(7) are called the dynamical normal modes. It is also of interest to study the effects of gravitational radiation reaction, which may produce the so-called secular

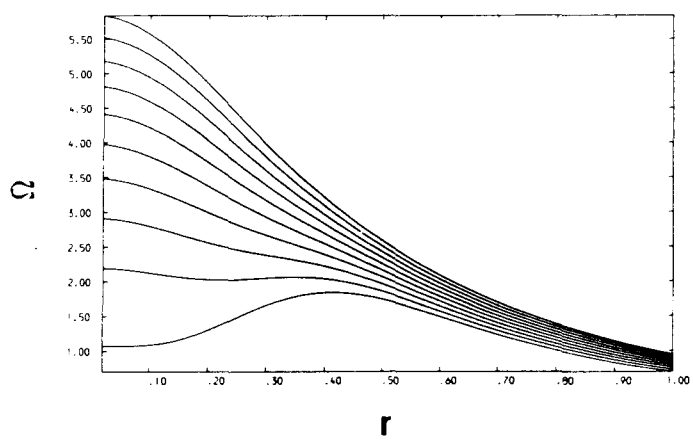

Figure 2. Angular velocity curves for several representative unperturbed discs. The values of the ratio τ of kinetic to potential energy of the displayed discs are listed in Table 1. Note that $\Omega(r)$ is a monotonically increasing function of τ.

instability. We shall determine the changes in the dynamical eigenfrequencies by eigenvalue perturbation theory, as described by Schutz (1980b). Previous analytic work (see Comins 1979 for a summary) leads us to expect that the secular instability in a mode will set in along a sequence as its frequency passes through zero. This is borne out by our calculations, which also support the 'explanation' of the instability given by Friedman & Schutz (1978b) in terms of the energy of the mode. These results are presented in Section 7 below.

Previous work gives us much less idea of what to expect of the general behaviour of the dynamical modes along the sequence, because this seems to be the first differentially rotating sequence to be studied in this detail. But from studies of the Maclaurin spheroids (Lyttleton 1953; Chandrasekhar 1969), of the simplest Bardeen discs (Paper I), and of local wave theory (Papaloizou & Pringle 1978) we think one could reasonably expect the following features.

(i) For the isentropic discs we study there should be two kinds of modes: the analogues of the p-modes of non-rotating stars (Ledoux & Walraven 1958), and the Rossby modes, the analogues of the toroidal modes of non-rotating stars. (Our Rossby modes are named by analogy with certain modes of incompressible fluids. See Greenspan 1968, p. 89.)

(ii) Instead of the eigenfrequency ω of a mode, it is physically preferable to use its *pattern speed*,

$$\omega_p = -\omega/m, \tag{8}$$

which is the angular velocity of surfaces of constant phase of the perturbation. In non-rotating stars, the usual eigenvalue is ω^2, so eigenfrequencies come in the pairs $\pm(\omega^2)^{1/2}$ These have identical eigenfunctions and equal but opposite pattern speeds.* For the p-mode analogues in our discs we should expect rotation to 'split' these modes: we should still expect pairs with roughly similar eigenfunctions and with pattern speeds on either side of some mean angular velocity of the disc. The shorter-wavelength p-modes should have pattern speeds further from the mean angular velocity.

(iii) As in Paper I, the Rossby modes, or r-modes, should form a single sequence of pattern speeds decreasing to an accumulation point. If their eigenfunctions tend to accumulate in the outer regions of the disc, then the accumulation point might be the angular velocity of the rim.

(iv) The big unknown is the continuous spectrum of pattern speeds covering the range of Ω in the disc. Such modes have corotation points, and their eigenfunctions may exhibit singular behaviour. This has not received much attention in the literature (*cf.* Hunter 1969; Balbinski 1982), but our finite-dimensional numerical approximation will give at best only an indication of the true behaviour, since no finite-dimensional problem can have a continuous spectrum. Thus, when we refer below to the 'continuous spectrum', we mean the region where we expect the exact problem to have a continuous spectrum. We should certainly expect the r-modes to be in this region for short enough wavelength, and it may also happen that at least some p-modes will also be found there. This expectation is supported by examining the Maclaurin sequence, along which the 'bar mode' – the analogue of our fundamental p-mode – goes from pattern speeds larger than Ω to speeds smaller than Ω before going unstable. In our case, this would mean passing though at least part of the range of Ω in the star, i.e. being in the continuous spectrum.

These expectations are largely borne out by our calculations, as we shall see in Sections 5–6. We shall first, however, need to describe the method of calculation in more detail.

* Readers more familiar with modes of non-rotating stars should bear in mind two crucial differences: here the eigenvalue is necessarily ω, not ω^2; and the spherical harmonic index l no longer usefully characterizes modes, although m remains an eigenvalue.

3 Description of the numerical approach

In order to solve equations (5)–(7) we follow Bardeen (1975) by using the even Legendre functions $P^m_{2l+m}(\eta)$, where $\eta = (1-r^2)^{1/2}$, as a basis for expanding the dynamical perturbations for fixed m. For the uniform-density, rigidly rotating disc these are exactly the eigenfunctions (Paper I), and they have the advantage that they automatically satisfy the boundary conditions at the centre and edge of the disc. For the $n = 2$ polytropic discs under consideration here, it is convenient to expand

$$\delta\sigma/\eta = \exp(im\phi) \sum_{l=0}^{\infty} c_l P^m_{2l+m}(\eta); \tag{9}$$

to represent the perturbed velocity in terms of potentials

$$\delta \mathbf{v} = i\nabla[A(\eta)\exp(im\phi)] + \mathbf{e}_z \times \nabla[B(\eta)\exp(im\phi)], \tag{10}$$

or equivalently

$$\delta v = -i\left[\frac{r}{\eta}\frac{dA}{d\eta} + \frac{m}{r}B\right], \qquad \delta\Omega = -\left[\frac{1}{\eta}\frac{dB}{d\eta} + \frac{m}{r^2}A\right]; \tag{11}$$

and to expand A and B in terms of the Legendre functions, with coefficients A_l and B_l respectively:

$$A = \sum_{l=0}^{\infty} A_l P^m_{2l+m}(\eta), \qquad B = \sum_{l=0}^{\infty} B_l P^m_{2l+m}(\eta). \tag{12}$$

By using these expansions in equations (5)–(7), solving equation (3) for $\delta\nu_c$ in terms of the Legendre functions (Hunter 1963), multiplying (5)–(7) by $P^m_{2j+m}(\eta)$ and integrating over the range $0 \leqslant \eta \leqslant 1$, we can write the perturbation equations in the form

$$\sum_{k=0}^{\infty} C_{jk}\, d_k = i\omega\, d_j, \tag{13}$$

where the coefficients C_{jk} depend only on the equilibrium structure of the disc, and the vector $\{d_j\}$ has as components $\{c_i, i = 0, \ldots; A_i, i = 0, \ldots; B_i, i = 0, \ldots\}$.

Equation (13) is the basic eigenvalue problem for ω. The matrix C_{jk} whose eigenvalues we seek is not Hermitian. For a given disc the matrix elements C_{jk} must be determined numerically. The eigenvalue problem must also be solved numerically, and this forces us to truncate the problem at some order N, i.e. to solve

$$\sum_{k=0}^{N} C_{jk}\, d_k = i\omega\, d_j. \tag{14}$$

The faithfulness with which solutions of equation (14) represent solutions of (13) depends on the accuracy with with we can represent the different eigenfunctions with Legendre functions up to order $2N + m$. In general, we should not expect good representations for eigenfunctions with very short wavelengths or with singular behaviour.

Because C_{jk} is non-Hermitian, we must distinguish between right- and left-eigenvectors (Schutz 1980a). To make this important distinction explicit, we will write the truncated problem (14) in the form

$$C|r\rangle = i\omega|r\rangle \tag{15}$$

for the right-eigenvector $|r\rangle$, and similarly

$$\langle l|C = i\omega\langle l|, \tag{16}$$

for the left-eigenvector $<l|$. In the appendix to Paper I is shown how to obtain the left-eigenvector directly from the right-eigenvector without solving equation (16).

Most of our computations have been done with $N = 15$, which is enough to represent eigenfunctions with fairly small wavelengths; for comparison, some modes have been computed using $N = 30$. We will consider the accuracy of these truncations in some detail below. The most time-consuming step is the evaluation of all $3(N+1)$ eigenvalues of equation (14). We have used an ICL 2980, on which the evaluation of the eigenfrequencies and some selected eigenvectors takes about 30 s of computer time for an $N = 15$ model. Many of our figures have been plotted by the DIMFILM microfilm package on the University of London's CDC 7600.

4 Equilibrium sequence

The sequence of equilibrium models is calculated in the same manner as Bardeen (1975). We choose a particular surface density σ, which is common to all members of the sequence (Fig. 1). Then by changing the parameter κ in equation (2), we construct a whole range of models from very hot and thick models to cooler, thinner ones. Equation (2) forces a regularity condition on σ near the edge of the disc: if $\sigma \sim \eta^k$ as $\eta \to 0$ then $k \geqslant 3$. We take $k = 3$.

We have evaluated 45 models, ranging from the warmest with $\tau = 0.1178$ (recall that τ denotes the ratio of kinetic to potential energy) to the coldest with $\tau = 0.3676$. In Table 1 we list some properties of 10 of these models: τ, the 'mean' angular velocity J/I (angular momentum divided by moment of inertia) and J/M. The angular velocity distribution for these models is given in Fig. 2. The smaller the pressure and thickness are, the stronger the differential rotation becomes. It is worth noting that, in the two hottest models represented, the angular velocity is not monotonically decreasing outwards from the centre, and therefore more than one corotation radius can exist for some frequencies. It is also apparent from Fig. 2 that we cannot make models much hotter than our hottest one, for eventually Ω reaches

Table 1. Ratios of kinetic to potential energies (τ), of angular momentum (J) to moment of inertia (I), and of angular momentum to mass (M) for the discs displayed in Fig. 2. The ratio J/I may be regarded as the mean angular velocity of the disc. The units are such that the mass and radius of the disc equal unity.

z	J/I	J/M
0.1186	1.494	0.210
0.1499	1.687	0.237
0.1803	1.848	0.260
0.2090	1.993	0.281
0.2380	2.125	0.299
0.2656	2.248	0.317
0.2923	2.365	0.333
0.3181	2.475	0.348
0.3433	2.580	0.363
0.3676	2.680	0.377

can imagine tracing individual modes back along this extended sequence from the non-rotating star up to our computed differentially rotating models.

When $\Omega = 0$ there are three kinds of modes, two of which are trivial. There are p-modes, which come in pairs $\pm\omega_p$ (i.e. equally distant from $\omega_p = 0$) and have $|\omega| \to \infty$ as their wavelength decreases. There are g-modes, which in our discs all have zero frequency since we take the adiabatic index to be equal to $1 + 1/n = 3/2$. This is true as well for the rotating discs, so we shall ignore the g-mode analogues in our later discussion. Finally, the non-rotating star also has an infinite number of zero-frequency toroidal modes, which physically correspond to setting the star into slow rotation.

When rigid rotation is introduced, the p-modes are 'dragged', appearing again in pairs whose two values of ω_p are roughly equidistant from Ω, for small Ω, and with $|\omega_p| \to \infty$ as their wavelength decreases. As Ω increases, we see from Paper I that paired p-modes begin to approach each other in frequency and eventually acquire the same ω_p, at which point they go unstable. This is somewhat complicated in our case by the differential rotation and the fact that these modes have corotation points (see the next paragraph), but the general picture is similar to that in Paper I. By contrast, the r-modes occur singly rather than in pairs, they are always stable in the Ω = constant discs, they span only a finite range of ω_p, and for small wavelengths $\omega_p \simeq \Omega(1 + 1/2l^2)$, where l is index of the mode associated with the Legendre polynomical $P^m_{2l+m}(\eta)$. Paper I gives a discussion of these modes. This general pattern for the r-modes is also evident in the cold disc models of Hunter (1972) and in the local calculations of Papaloizou & Pringle (1978).

When we introduce differential rotation, the main complication for the r-modes is the corotation region. Outside this region, the familiar pattern prevails, and in Fig. 4 we have

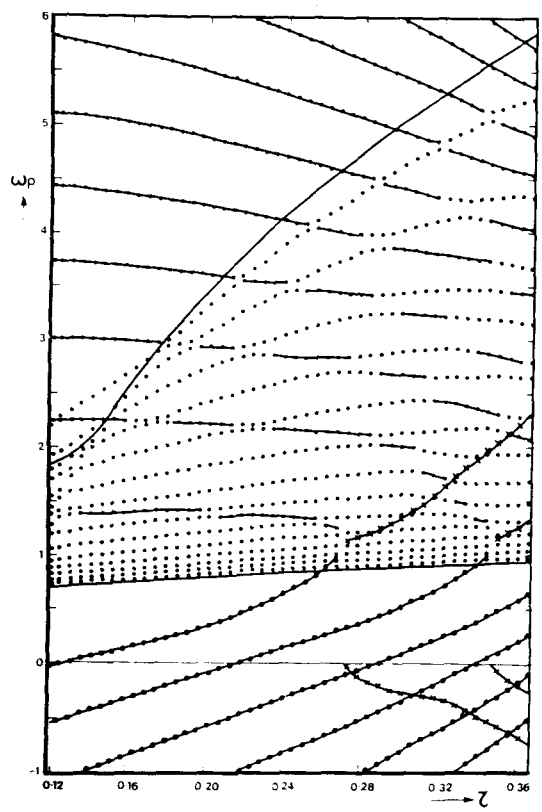

Figure 4. As Fig. 3, but dots have been joined into sequences which we believe represent the progress of the p-mode eigenfrequencies as τ increases. Where we have found mixed-type modes, near 'bumping' points, we have not joined them to any sequence. Membership of sequences becomes less certain the further one goes into the corotation region.

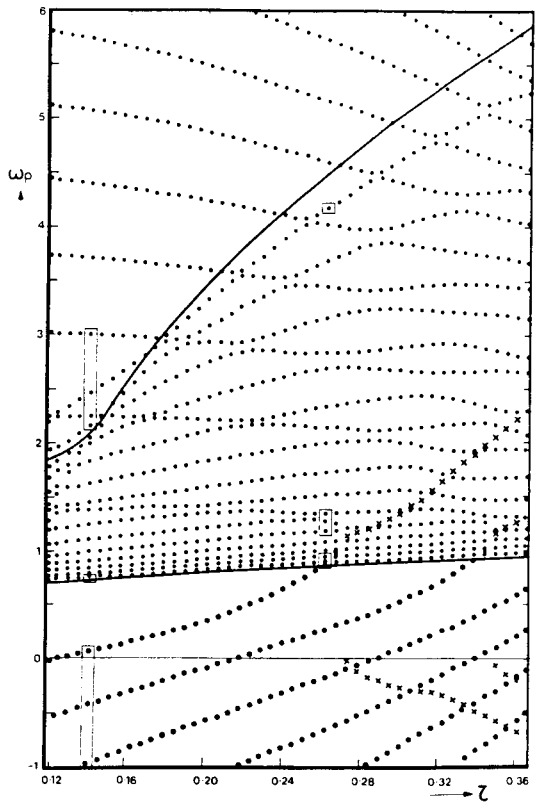

Figure 3. Pattern speeds of normal modes for $m = 2$ as functions of τ, the ratio of kinetic to potential energy of the unperturbed model. Each dot is a computed eigenfrequency. Crosses represent the real (above $\omega_p = 0$) and imaginary (below $\omega_p = 0$) parts of $(-\omega/m)$ for modes with complex eigenfrequencies. The two solid curves are the maximum and minimum values of Ω inside the discs. Boxed modes are examined in Figs 5–8.

zero at some radius; a thicker model would require an inward-pointing centrifugal force! So our sequence terminates before it reaches zero angular momentum.

5 Spectrum of eigenfrequencies

In Fig. 3 the pattern speeds (equation 8) of most of the modes for $m = 2$ are plotted against the value of τ for the equilibrium model. The continuous lines denote the largest and smallest values of Ω in the disc, so modes between them have corotation points, i.e. places in the disc where Ω equals ω_p. This region will be called the *corotation region.* It naturally expands as the differential rotation increases with τ. The points represented by crosses are the real and imaginary parts of the frequencies of dynamically unstable modes, divided by $-m$. The imaginary parts are represented in the negative pattern-speed region for clarity, but the complex frequencies come in complex–conjugate pairs.

All the points in Fig. 3 have been calculated for $N = 15$. For modes outside the corotation region, this is large enough to get a good representation for all but the largest pattern speeds. But the pattern speeds inside the corotation region turn out to be less well defined (i.e. change more substantially with N), and we shall return to this point later on.

In order to make sense of the spectrum, it is useful to imagine extending our sequence by adding another sequence of models from $\tau = 0.12$ down to some small τ, with decreasing corotation region. (As we remarked earlier, this can not be accomplished without changing the surface density distribution.) Eventually this hypothetical sequence reaches a model with null corotation region: a uniformly rotating model. Then we can join at that point yet another sequence, this time of constant-Ω models, extending down to $\Omega = \tau = 0$. Now we

joined with solid lines those sequences of eigenfrequencies of Fig. 3 which seem to correspond to the same modes as rotation increases. The p-modes are clearly behaving as expected, and we can even see two discrete r-modes outside the corotation region in our low-τ models. These r-modes are distinguished from the p-modes by the fact that their ω_p increases nearly as fast as the maximum Ω does, while the p-mode $|\omega_p|$ decreases monotonically with τ.

Inside the corotation region we have mainly the r-modes. These comprise roughly one-third of all the modes in the models (they are a larger fraction in Figs 3 and 4, since the high-frequency p-modes are not displayed) and seem to accumulate at the minimum Ω. In contrast to the modes outside the corotation region, these modes suffer severe truncation effects: their eigenfunctions are not well represented when $N = 15$ and do not converge any better even when $N = 30$. This is related to another fact, that when N is changed there is a relatively large change in the frequency of a mode in the corotation compared to what happens outside. The relation between these two is discussed in the Appendix, where we give a precise characterization of the truncation error. Table 2 presents the computed spectra for the model with $\tau = 0.3181$ for $N = 15$ and $N = 30$. Two things are striking: (i) for p-modes the principal change from $N = 15$ to 30 is the addition of higher values of $|\omega_p|$ (although there is some 'filling-in', particularly for $\omega_p > 0$), while the eigenfrequencies already present at $N = 15$ do not change very much; (ii) for r-modes, there is a general filling-in of the corotation region, and it is hard to identify the $N = 15$ modes in the $N = 30$ spectrum. This filling-in is not what one would expect for the rigidly rotating disc, where the increase in N should simply add shorter-wavelength r-modes, all of which would be near the accumulation point. What we appear to be seeing here is the numerical attempt to represent the *continuous spectrum*: the shear of differential rotation means that every ω_p in the corotation region is actually in the spectrum of the exact problem $N = \infty$, so that increasing the accuracy from $N = 15$ to $N = 30$ results in a denser spacing of modes in the corotation region. Points of the continuous spectrum do not have proper (i.e. twice differentiable) eigenfunctions (Riesz & Sz.-Nagy 1955), and for this region the truncation effects may be severe even for r-modes far from the accumulation point.

Nevertheless, not all modes in the corotation region are r-modes, for some p-modes clearly enter that region. It appears that these modes keep their identity to some degree: their truncation problems are less severe, particularly near the lower edge of the region, and the two lowest-order pairs manage to 'find' their partners in the corotation region, join and go unstable. We have joined with solid lines those points in Fig. 4 which we feel represent the progress of the p-mode in this region. With infinite accuracy the calculation would probably reveal a smooth progress of a p-mode through the continuous spectrum. In our truncated problem, there seems to be some interference between p- and r-modes. As τ increases, r-modes tend to have increasing ω_p, p-modes decreasing. This would lead to crossing of modes and degeneracy. The problem actually seems to avoid this degeneracy by 'bumping', several examples of which can be seen in Fig. 4. At a bump, the r- and p-modes seem to exchange character. This is most likely an artefact of our finite precision. Many of the properties of the continuous spectrum, such as the possible existence of true eigenvalues inside it, come out clearly in the recent study by Balbinski (1982), who develops projection operators for the continuous spectrum's 'eigenfunctions'.

6 Eigenfunctions

Fig. 4 and Table 2 provide strong evidence for two qualitatively different classes of modes, which we have called p- and r-modes; we will now see that the eigenfunctions of the two

Table 2. Comparison of pattern speeds of the truncated problem, equation (14), for the normal accuracy ($N = 15$) and increased accuracy ($N = 30$) in the disc with $\tau = 0.3181$. Each mode for $N = 15$ is listed next to that for $N = 30$ whose eigenfrequency is closest. The modes with corotation points lie between the dashed lines. Note the uniform filling-in of this region as N is increased, by contrast with the rest of the table. There is also a pair of complex-frequency modes listed at the end. Asterisks (*) denote modes we have identified as $p^{\pm}$ modes inside the corotation region in Fig. 4. Particularly near the top of the corotation region, these eigenfrequencies change less with N than those of nearby r-modes. The identifications are much less certain for the lower pattern speeds.

$N = 30$	$N = 15$	$N = 30$	$N = 15$	$N = 30$	$N = 15$	$N = 30$	$N = 15$
30.450		5.361230	5.361135	1.419	1.380	−3.542409	−3.542474
25.469		5.060		1.338		−4.028962	−4.028317
22.076		4.869	4.867*	1.266	1.247	−4.517	−4.494
19.551		4.816	4.741	1.202		−5.006	−4.910
17.607		4.519		1.146	1.138	−5.497	−5.664
16.075	15.525	4.353	4.360*	1.097		−5.988	
14.840		4.158	4.084	1.054	1.053	−6.479	
13.827		3.880	3.819*	1.018		−6.972	
12.990		3.756		0.987	0.989	−7.464	
12.309		3.485	3.455	0.961		−7.957	
11.785	11.894	3.298	3.231*	0.940	0.944	−8.451	−8.568
11.341		3.126		0.924		−8.944	
10.865		2.911	2.908	0.912	0.915	−9.426	
10.368		2.728		0.904		−9.868	
9.869	9.781	2.587	2.656	0.616226	0.616226	−10.353	
9.370		2.426	2.433*	0.173376	0.173376	−11.029	
8.870		2.250		−0.245312	−0.245312	−11.933	
8.369	8.393	2.097	2.146	−0.690669	−0.690670	−13.165	
7.869		1.972	1.972	−1.150819	−1.150821	−14.928	
7.368	7.433	1.868		−1.620226	−1.620230	−17.556	
6.866	6.777	1.739	1.766*	−2.095292	−2.095300	−22.089	
6.364	6.325	1.619		−2.574958	−2.574976	(1.468355	(1.468358
5.862424	5.859188	1.512	1.548	−3.057619	−3.057659	± 0.293788)	± 0.293784)

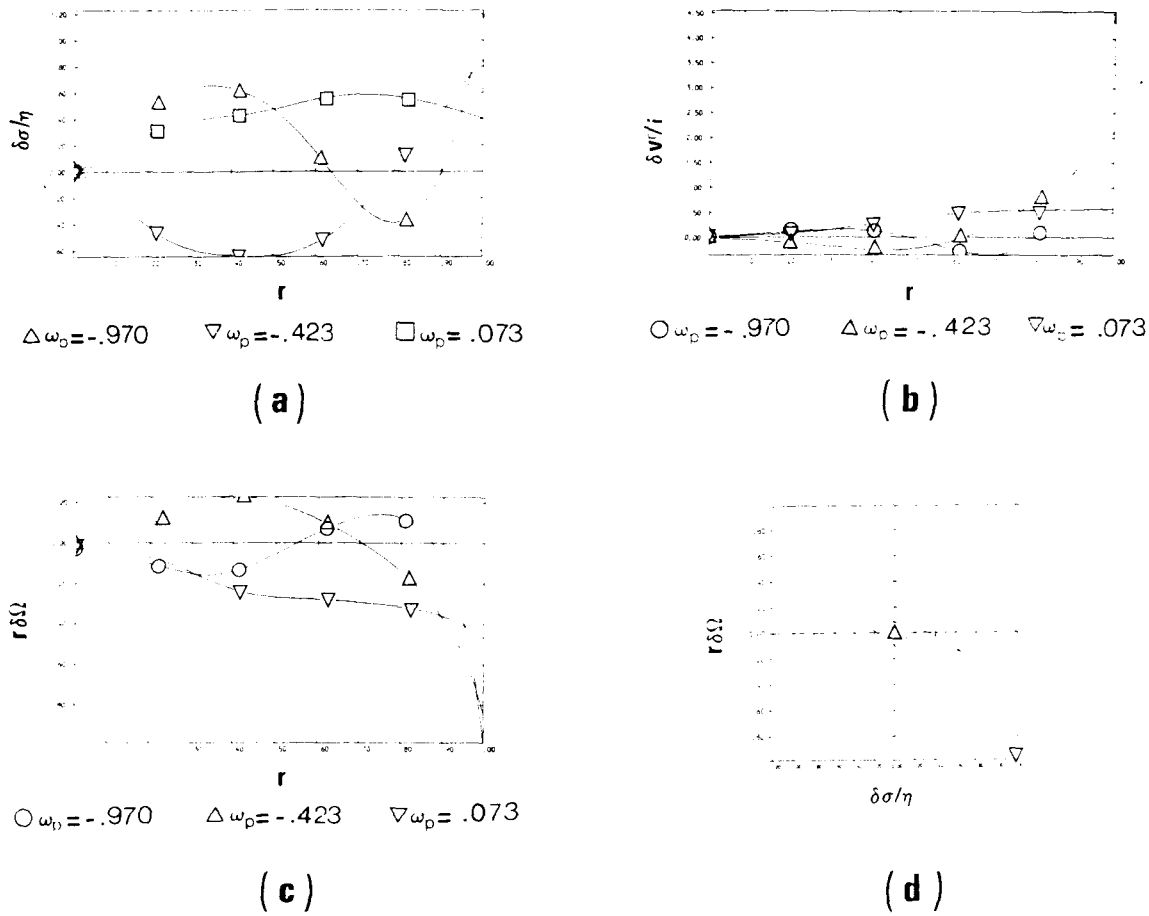

Figure 5. Eigenfunctions and a phase diagram for modes of a 'slow' model, $\tau = 0.1437$. The perturbations in the surface density ($\delta\sigma/\eta$), radial velocity ($\delta v^r/i$) and angular velocity ($r\delta\Omega$) are displayed in (a)–(c), respectively. The vertical scales are arbitrary, but note that for any single mode the ratio of two perturbations (e.g. $\delta\Omega/\delta\sigma$) is independent of normalization. In (d) we plot a phase diagram, of $r\delta\Omega$ versus $\delta\sigma/\eta$, for one mode. For the interpretation of Figs 5–8, see text.

classes are also qualitatively different, sometimes strikingly so even when modes of the two classes are near each other in eigenfrequency. Our eigenfunction plots in Figs 5–8 are of two kinds: (i) plots of perturbations* $\delta\sigma/\eta$, $\delta v^r/i$, or $r\delta\Omega$ versus r, in which r runs from 0 to 1 and the normalization of the eigenfunctions is arbitrary; and (ii) phase diagrams, which are plots of $\delta\sigma/\eta$ versus $r\delta\Omega$, parametrized by r, in which both scales are arbitrary. Phase diagrams of this type are useful in non-rotating stars for distinguishing between p-modes and g-modes, based upon the sense of rotation (clockwise or counter-clockwise) of the curve. In our problem we have similarly only one independent variable (r), so we may hope that phase diagrams will also be useful here. There are three possible diagrams for each mode, according to which pair of the variables ($\delta\sigma$, δv^r, $\delta\Omega$) is chosen. By experimenting with all three pairs we have found that the pair ($\delta\sigma$, $\delta\Omega$) seems to give the best diagram: it is generally a more open curve and it seems to show systematic trends better.

The eigenfunctions are chosen from two different models: a slowly rotating model with $\tau = 0.1437$, and a faster one, just near the onset of dynamical instability, with $\tau = 0.2710$. Fig. 5 shows three typical p-modes, the lowest-order counter-rotating p-modes of the slow

* For real-frequency modes, it is possible to choose $\delta\sigma$ in equations (5)–(7) to be real. Then $\delta\Omega$ is also real and δv^r pure imaginary. The eigenfunction plots therefore give the amplitude of the perturbations.

disc. The fundamental mode has $\omega_p = 0.073$, so it is rotating forwards with respect to the inertial frame but backwards with respect to any part of the disc. Its eigenfunctions have no nodes. The first and second 'overtones' have frequencies -0.423 and -0.970 respectively (i.e. further from the mean angular velocity of the disc), and their eigenfunctions have 1 and 2 nodes, respectively. All this is qualitatively the same as for p-modes of spherical stars. The phase diagram, for the second overtone, Fig. 5(d), winds counter-clockwise one full turn (i.e., ending in the same quadrant in which it began). It thus has a winding number $+1$. The fundamental's phase diagram has winding number 0 and the first overtone has 1/2 (i.e. it travels counter-clockwise through only two quadrants). Again, this behaviour is familiar from non-rotating stars (*cf.* Unno *et al.* 1979).

Fig. 6 displays the forward-going counterparts of the first and second p-modes of Fig. 5 for the slow model as well as two r-modes outside the continuous spectrum. (The forward-going fundamental p-mode in this model already has a corotation point. We shall look at such modes in the fast model below.) The p-modes, so classified because they are on descending sequences in Fig. 4, are those with $\omega_p = 2.253$ and $\omega_p = 3.004$. The r-modes, on ascending sequences, are $\omega_p = 2.168$ and $\omega_p = 2.469$. Thus, the r-modes alternate with the p-modes as the frequency increases; nevertheless, the two r-modes have eigenfunctions which resemble each other much more than they resemble the p-modes, and vice versa. This confirms the classification of the modes. The p-modes have 1 and 2 nodes for $\omega_p = 2.253$

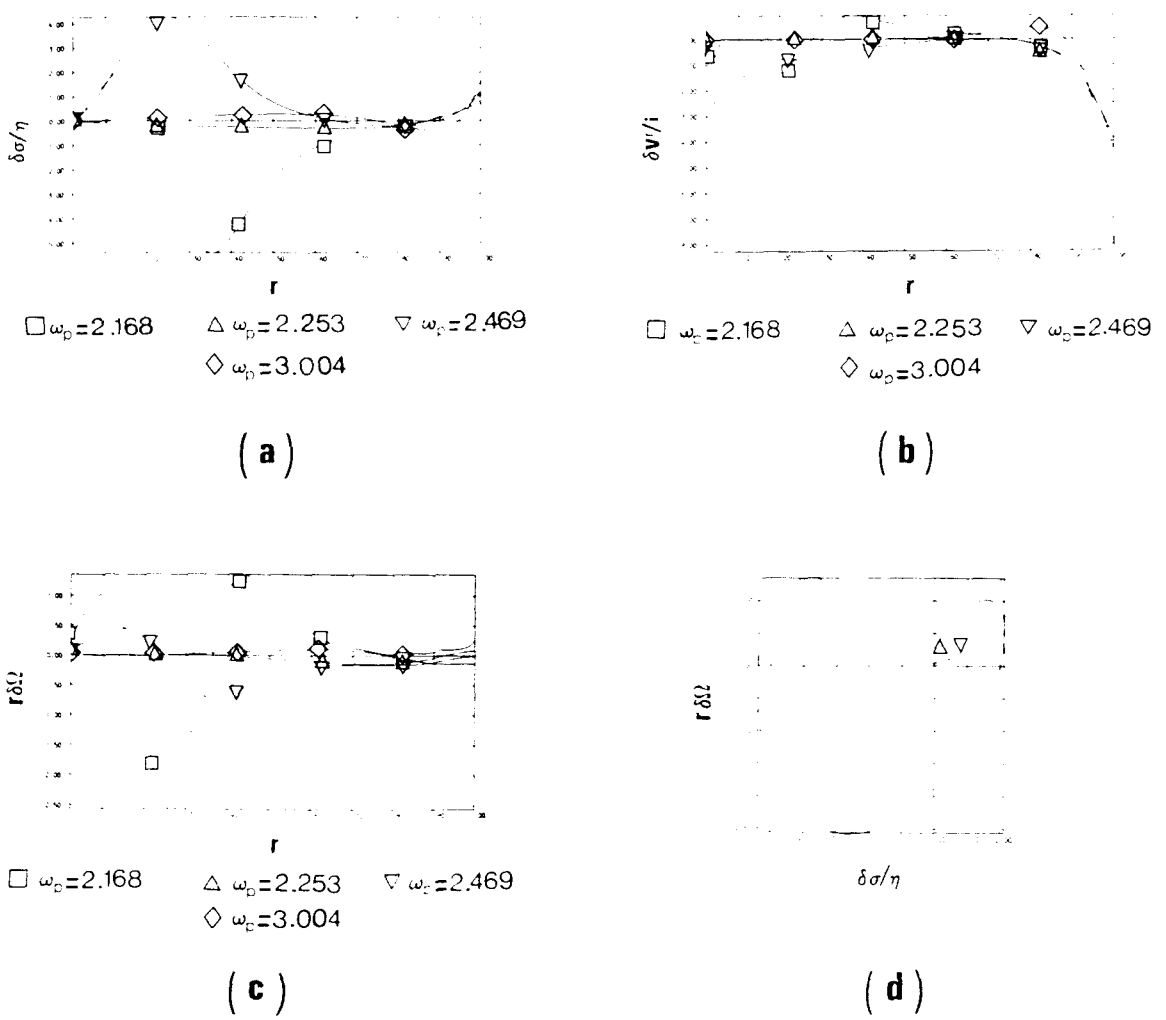

Figure 6. As Fig. 5 for four other modes of the same model.

and 3.004, respectively, as one expects. The r-modes have somewhat less regular behaviour: the number of nodes is not the same for each eigenfunction of a single frequency, and the trend in numbers of nodes is not clear. But the phase diagrams help considerably. Fig. 6(d) shows this for $\omega_p = 2.168$. Its winding number, as defined above, is -1: one full clockwise turn. That for $\omega_p = 2.469$, which is not shown, also winds clockwise, but through only one quadrant, a winding number $-1/4$. We are thus inclinded to classify $\omega_p = 2.469$ as the *first* r-mode and $\omega_p = 2.168$ as the second. This accords with the uniformly rotating case, where ω_p decreases as the order of the r-mode increases.

Based on these examples, we shall introduce a shorthand for referring to modes. For example, mode $2p^+$ is the second-overtone forward-going p-mode, $0p^-$ the backward fundamental p-mode, etc. The mode $1r$ is the first Rossby mode ($\omega_p = 2.469$ above), while the r-mode of next highest frequency is $2r$, etc. The character of the mode (p or r) is defined by its phase diagram (counter-clockwise or clockwise rotation, respectively), while the order is defined by the ordering of frequencies: for $p^\pm$ modes, $np^\pm$ has a lower ω_p than $(n \pm 1)p^\pm$, while for r modes, nr is lower than $(n-1)r$. For p-modes this ordering should hopefully follow the number of nodes and the winding number, while for r-modes it should at least follow the winding number. Classifying a p-mode as p^+ or p^- is easy if the mode has no corotation point; otherwise we shall do it by following the mode along a sequence, as in Fig. 4.*

For the fast model we show in Figs 7–8 eigenfunctions whose pattern speeds are in the corotation region. This model is of interest because it is near the point of dynamical instability, which occurs when the $0p^\pm$ modes converge to become unstable (*cf.* Fig. 4). The eigenfunctions of the two branches of the fundamental, $0p^-$ ($\omega_p = 0.890$) and $0p^+$ ($\omega_p = 1.272$), are shown in Figs 7 and 8, respectively. On the whole, their eigenfunctions are similar, although it is notable that they no longer have nodes. The $0p^-$ mode has just entered the corotation region, yet it is clearly distinguished from the other two modes in Fig. 7, high-order r-modes with pattern speeds very close to that of $0p^-$: $\omega_p = 0.867$ and 0.895. A typical phase diagram for a high-order r-mode is also shown in this figure. This phase diagram is for a mode in the slow model, but it is essentially the same in the fast one. It winds clockwise, and it shows a characteristic feature of these high-order r-modes, that their dominant amplitude is near the edge of the disc. This compresses all the winding in the phase diagram to a small corner. In Fig. 7(a, b) it is also evident that $\omega_p = 0.867$ and $\omega_p = 0.895$ show this high-amplitude tendency for $\delta\sigma$ and δv^r near the edge. The $0p^-$ mode shows none of this. The r-mode at $\omega_p = 0.895$, which is very close to the $0p^-$ frequency 0.890, shows a tendency to high amplitudes in the main part of the disc: this is uncharacteristic of r-modes and probably reflects a 'mixing' due to the closeness of the two eigenfrequencies and the finite numerical precision. In Fig. 7(c) the scale is dominated by the behaviour of the two r-modes at the edge, where both become large, especially 0.867. The $0p^-$ mode is hardly distinguishable from zero on this scale. This illustrates another characteristic of the r-modes: $\delta\Omega/\delta\sigma$ (which is independent of normalization) is much larger than for p-modes.

The other branch of the fundamental of the fast disc ($\omega_p = 1.272$ in Fig. 8) is more difficult to distinguish from neighbouring r-modes, possibly because it lies further inside the

* There may be another method, namely using the sign of the mode's canonical angular momentum, but at present we do not know how to resolve the 'trivials' ambiguity for modes with corotation points (Friedman & Schutz 1978a) and so we cannot yet define the canonical angular momentum. Nevertheless, we feel that the classification into p^+ or p^- should be intrinsic to the model having those modes: it should not require knowing the behaviour of the mode along one of the infinite number of sequences of discs which contain that particular model.

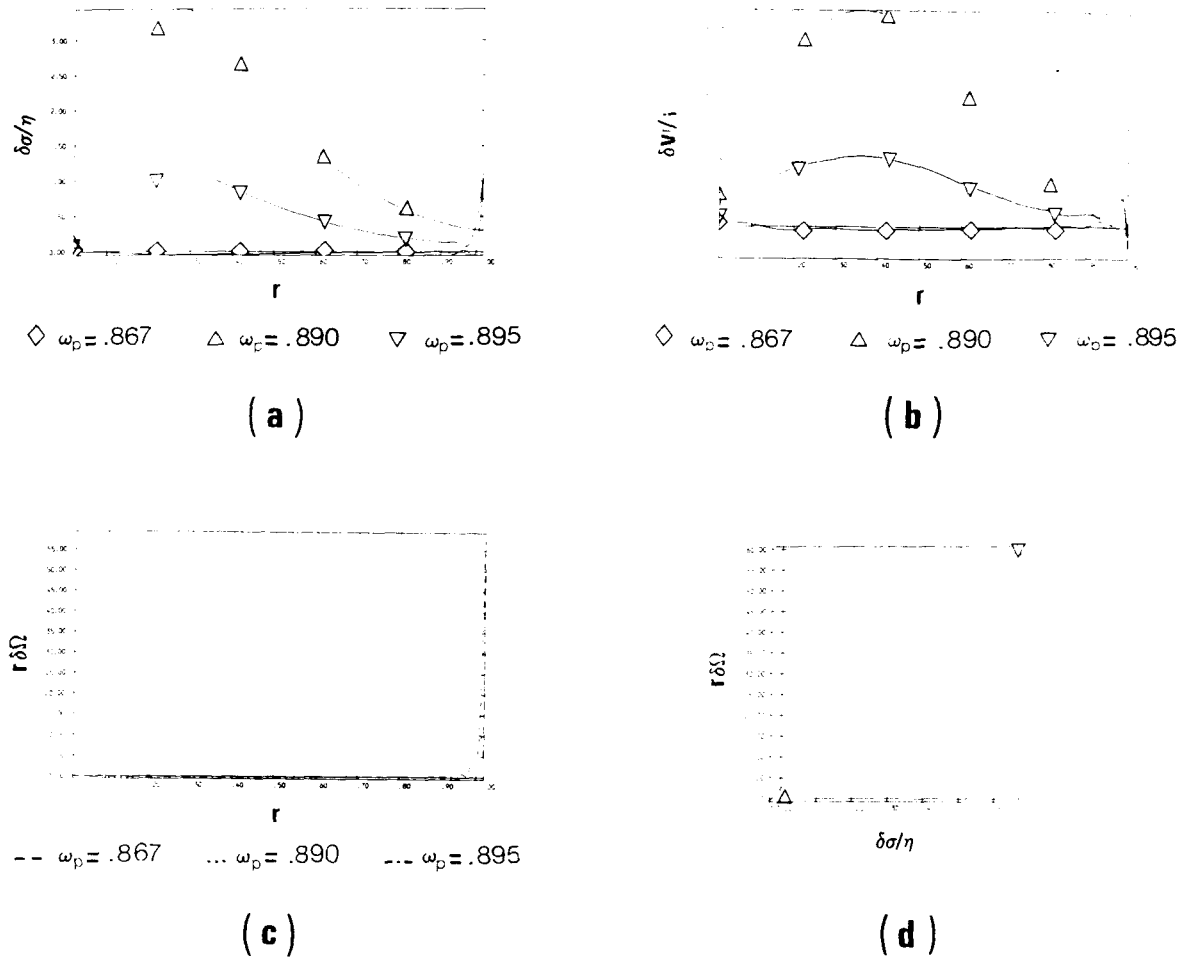

Figure 7. (a)–(c): As Fig. 5 for three modes of the 'fast' model, $\tau = 0.2710$. In (c) the candidate for the $0p^-$ mode, $\omega_p = 0.890$, is indistinguishable from zero on this scale. (d) The phase diagram of a typical high-order r-mode, taken from the 'slow' model.

corotation region. We can guess where it is by following the sequence of modes in Fig. 4. The pattern speeds of p^+ modes tend to decrease as the angular velocity increases along our sequence, while those of r-modes increase. In the region of the continuous spectrum, our numerical method can distinguish only the general features of p- and r-modes: some modes seem typical of one type or the other, but many modes have a mixed character, which we discuss below. We feel that the mode with $\omega_p = 1.272$ is the best candidate for the $0p^+$ mode, while the nearby $\omega_p = 1.179$ and $\omega_p = 1.344$ modes are r-modes. But these r-modes seem to share many p-mode features in their eigenfunctions.

This mixed character is also illustrated in Fig. 8(d), which shows the phase diagram of the fast disc's $1r$ mode, the continuation of the $1r$ mode of Fig. 6 into the corotation region. It starts near the centre of the disc as typical r-mode (clockwise) and ends near the edge as a typical p-mode (counter-clockwise). This mixed character may be due to the fact that the frequency of this mode is very near the frequency of the $4p^+$ mode, i.e. very near a 'bumping' point of the type discussed below.

Physically one might expect the long-wavelength p- and r-modes to be the most important for stability, as they have more coherent changes in density in the inner parts of the disc where the mass is concentrated. Short wavelength modes of both types tend to have significant amplitudes near the edge of the disc. The most important modes for stability,

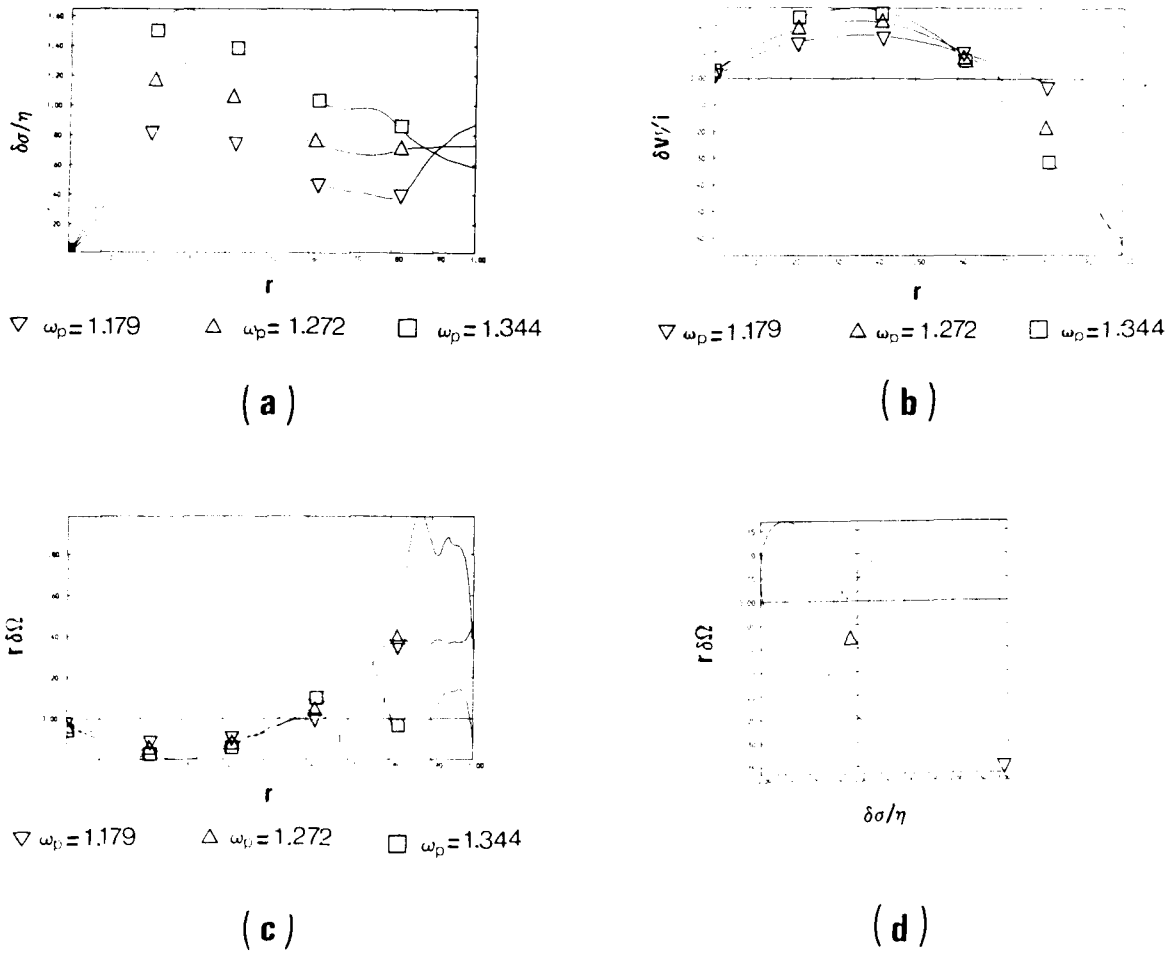

Figure 8. (a)–(c): As Fig. 5 for three modes of the 'fast' model. (d) Phase diagram of the $1r$ mode of the same model.

either dynamical (as in Fig. 4) or secular (as in the next section) are the $0p^{\pm}$ modes. Their amplitudes tend to get larger in the centre as the angular velocity increases (compare Fig. 5 with Fig. 7). After $\tau \approx 0.27$ these become dynamically unstable. A much more precise determination of the marginal instability point is not possible because of the inaccuracy of the eigenfunctions in the corotation region. By contrast, we have not seen any instabilities in the r-modes.

An obvious feature of Fig. 4 is mode 'bumping', where two modes seem to approach each other's eigenfrequencies, then turn away. It must be stressed that the classification of a mode as a p- or r-mode can and does change at such avoided crossings, even when they occur outside the continuous spectrum. Thus, the classification is physically useful but mathematically somewhat ambiguous.

7 Secular instability to gravitational radiation

There is a general criterion for the onset of secular instability to gravitational radiation (Friedman & Schutz 1978b) which says that secular instability will set in for a mode as its pattern speed changes from negative to positive along a sequence of models. Moreover, only the corotating modes going backwards with respect to the mean angular velocity of the disc

$(0 < \omega_p \lesssim \langle \Omega \rangle)$ are secularly unstable, or more precisely, only modes with negative canonical energy are secularly unstable. In this section we will explicitly calculate the effect of gravitational radiation on the frequency of some of the modes of our discs, and we will confirm the above picture in detail.

According to the standard formulation of the radiation reaction problem for a Newtonian system (*cf.* Misner, Thorne & Wheeler 1973) we can calculate the damping due to the radiation by adding to the Newtonian potential the 'reaction' potential $\nu_{(\mathrm{react})}$ given by

$$\nu_{(\mathrm{react})} = -\frac{G}{5c^5}\frac{d^5}{dt^5}(\text{ǂ}_{jk})x^j x^k, \tag{17}$$

where

$$\text{ǂ}_{jk} = I_{jk} - \frac{1}{3}\delta_{jk} I^l_l, \tag{18}$$

$$I_{jk} = \int \rho x_j x_k \, d^3x. \tag{19}$$

Only the perturbed density $\delta\sigma$ contributes to the radiation reaction. (The extra reaction corrections to the continuity equation, pointed out by Schutz 1980c, do not, as it turns out, affect the present calculation.) This reaction potential has a simple expansion in terms of the Legendre functions, by analogy with equation (12). If we write

$$\nu_{(\mathrm{react})} = \sum_{l=0}^{\infty} \nu_{(\mathrm{react})l} P^m_{2l+m}(\eta) \exp(im\phi), \tag{20}$$

then only one coefficient is non-zero for $m = 2$:

$$\nu_{(\mathrm{react})l} = -\frac{8\pi G}{525}\left(c_0 + \frac{10}{3}c_1\right)(i\omega/c)^5 \delta^0_l, \tag{21}$$

where c_0 and c_1 are the first coefficients in the expansion (9) of $\delta\sigma/\eta$ for $m = 2$. Note that modes with $m > 2$ do not couple to this potential because it takes account only of quadrupole gravitational radiation.

Because the reaction potential is of order $(v/c)^5$, we can treat it as a small perturbation on our original dynamical eigenvalue problem. The effect of $\nu_{(\mathrm{react})}$ is to change the matrix C in equation (13) by a matrix δC, and to change the eigenfrequency of a dynamical mode by a first-order 'secular' amount (*cf.* Schutz 1980b)

$$\delta\omega = -i\,\frac{\langle l|\delta C|r\rangle}{\langle l|r\rangle}, \tag{22}$$

where $\langle l|$ and $|r\rangle$ are, respectively, the left- and right-eigenvectors of the dynamical problem, equations (15) and (16). The results of Schutz (1980b) guarantee that $\langle l|r\rangle \neq 0$ except at points of marginal dynamical stability. A mode is said to be secularly unstable when $Im(\delta\omega) < 0$. Physically we can expect that the modes most affected by radiation should be the $0p$ modes, because they have the most coherent changes in density. Moreover, p-modes should be affected more than the r-modes; and the short wavelength modes, being less coherent, may be almost unaffected by radiation.

Unlike the determination of the marginal dynamical instability point, we can calculate with precision the onset of secular instability, which occurs at $\tau = 0.1221$ and coincides with the point where the $0p^-$ mode has zero frequency (a Dedekind-like mode).

Table 3. Secular instability to gravitational radiation in the $0p^-$ mode of the sequence. Column 1 is the ratio of kinetic to potential energy of the unperturbed disc; column 2 is the pattern speed, without radiation effects; column 3 is the change in the frequency produced by radiation (negative numbers represent exponential growth); column 4 is the mean value of the angular velocity, equation (23); and column 5 is the canonical angular momentum, following Friedman & Schutz (1978a). The last two have not been defined for modes with corotation points, as in the last row of the table. Numbers in brackets are powers of 10.

τ	ω_p	$Im\,\delta\omega \cdot c^5/G$	$\langle\Omega\rangle$	J_c
0.1186	−0.0116	0.507 (−10)	1.2488	−0.0474
0.1499	0.0953	−0.212 (−5)	1.3778	−0.0542
0.1803	0.2153	−0.140 (−3)	1.5363	−0.0640
0.2096	0.3599	−0.204 (−2)	1.7455	−0.0786
0.2380	0.5484	−0.189 (−1)	2.0131	−0.0964
0.2656	0.8176	−0.189 (0)	2.2374	−0.0946
0.2710	0.8900	−0.343 (0)	–	–

In Table 3 we show some of the results for the $0p^-$ mode. We follow it from a point where it is stable up to near the point of its dynamical instability. The last two columns show (i) the mean angular velocity of the disc when averaged over the mode's eigenfunction,

$$\langle\Omega\rangle = \int \sigma\Omega\,|\xi|^2\,d^2x \Big/ \int \sigma\,|\xi|^2\,d^2x, \tag{23}$$

where ξ is the canonical Lagrangian displacement eigenvector of the dynamical mode (Friedman & Schutz 1978a); and (ii) the canonical angular momentum J_c of the dynamical mode, as defined by Friedman & Schutz (1978a) in terms of ξ. (The canonical energy of these modes, E_c, is given by $E_c = \omega_p J_c$.) Table 3 illustrates the assertions made at the beginning of this section and confirm the criteria established in Friedman & Schutz (1978b). The canonical Lagrangian displacement vector ξ of the mode is easily obtained from the Eulerian perturbations. As Friedman & Schutz (1978b) point out, this displacement is automatically canonical if the mode has no corotation point, but not necessarily otherwise. We have not attempted to extend the analysis to modes whose eigenfrequencies are in the corotation region. See Balbinski (1982) for a calculation of E_c for the continuous spectrum.

The eigenfunctions of the $0p^-$ mode are displayed in Fig. 5 for $\tau = 0.1437$ and Fig. 7 for $\tau = 0.2710$. The pattern rotates in the same direction but more slowly than the background disc, and the density changes are largest in the inner regions. (Recall that $m = 2$, so we will have maximum growing density along a diameter and maximum decreasing density along a perpendicular diameter.) The radial velocity of this perturbation is outwards where $\delta\sigma > 0$ and inwards where $\delta\sigma < 0$. The change $\delta\Omega$ in the tangential velocity is negative where $\delta\sigma > 0$ and positive where $\delta\sigma < 0$. The whole disc tends towards a bar shape, with no spiral pattern since the mode is dynamically stable.

It is interesting to see how secular instability sets in the $1p^-$ mode (also when it reaches $\omega_p = 0$) in order to compare the effects of the radiation in it with the effects of the fundamental mode.

In Table 4 some values for this mode are shown. The same conclusions can be drawn for the higher p-modes, which become secularly unstable when their pattern speeds become zero and remain secularly unstable until the dynamical instability point. As the modes acquire more and more nodes, which tend also to concentrate near the edge of the disc, they become less and less affected by radiation.

Table 4. The same as Table 3 for the $1p^-$ mode. It goes secularly unstable at a larger value of τ than the $0p^-$ mode.

τ	ω_p	$Im\,\delta\omega \cdot c^5/G$	$\langle\Omega\rangle$	J_c
0.1186	−0.5440	0.383 (−3)	1.1632	−0.0271
0.1499	−0.3923	0.280 (−4)	1.2672	−0.0308
0.1803	−0.2382	0.379 (−8)	1.3471	−0.0349
0.2096	−0.0803	0.192 (−7)	1.4028	−0.0394
0.2380	0.0782	−0.895 (−7)	1.4480	−0.0448
0.2656	0.2387	−0.627 (−4)	1.5197	−0.0529
0.2923	0.4096	−0.173 (−2)	1.6490	−0.0659
0.3181	0.6162	−0.209 (−1)	1.8471	−0.0847
0.3433	0.9246	−0.302 (0)	1.9650	−0.0789

The p^+ modes are always secularly stable. Those with large wavelengths are the more damped by radiation and even when they enter the corotation region they are more strongly damped than nearby r-modes. Neither the discrete r-modes nor the r-modes in the corotation region are secularly unstable and they also follow the general pattern that the ones more strongly damped by gravitational radiation are the ones with larger wavelengths.

8 Conclusions

We have studied the normal modes of a particular sequence of rotating, compressible Bardeen fluid discs in some detail. It is usually possible to distinguish two classes of modes, which we have called p- and r-modes. Each disc has two branches of p-modes, and the stability of the disc seems to depend only on their properties. There is a single sequence of r-modes, and in discs with strong differential rotation most of them have corotation points. We believe that an exact (i.e. analytic) analysis would find that these r-modes are only numerical approximations to a continuous spectrum of modes. We find p-modes with corotation points as well, but these will probably remain discrete modes even in an analytic calculation. We find that the first secular instability to gravitational radiation sets in at $T/|W| = 0.1221$; the first dynamical instability occurs at $T/|W| \simeq 0.27$, and the p-modes involved have corotation points. The behaviour of the modes along the sequence is remarkably similar to the pattern for the Maclaurin sequence (Chandrasekhar 1969). The presence of strong differential rotation does not seem to have too much influence, nor does the compressibility of the disc. A number of question marks remain, particularly concerning the continuous spectrum and the reliability of the criteria that we have suggested for the classification of modes.

Acknowledgments

It is a pleasure to acknowledge the contribution of James Bardeen to this work, both in discussions and by supplying a computer program which formed the basis of these calculations. We have also benefited from many conversations with Manning Butterworth. One of us (EV) gratefully acknowledges the support of a fellowship from the Spanish Ministerio de Universidades e Investigation.

References

Bardeen, J. M., 1975. In *Dynamics of Stellar Systems, IAU Symp. 69*, ed. Hayli, A., Reidel, Dordrecht, Holland.

Balbinski, E., 1982. *PhD thesis*, University College Cardiff.
Chandrasekhar, S., 1969. *Ellipsoidal Figures of Equilibrium*, Yale University Press, New Haven.
Comins, N., 1979. *Mon. Not. R. astr. Soc.*, **189**, 233.
Friedman, J. L. & Schutz, B. F., 1978a. *Astrophys. J.*, **221**, 937.
Friedman, J. L. & Schutz, B. F., 1978b. *Astrophys. J.*, **222**, 281.
Greenspan, H. P., 1968. *The Theory of Rotating Fluids*, Cambridge University Press.
Hunter, C., 1963. *Mon. Not. R. astr. Soc.*, **126**, 23.
Hunter, C., 1969. *Studies Appl. Math.*, **48**, 55.
Hunter, C., 1972. *Ann. Rev. Fl. Mech.*, **219**.
Ledoux, P. & Walraven, Th., 1958. *Handb. der Physik*, **51**, 353.
Lyttleton, R. A., 1953. *The Stability of Rotating Liquid Masses*, Cambridge University Press.
Misner, C. W., Thorne, K. S. & Wheeler, J. A., 1973. *Gravitation*, W. H. Freeman and Co., San Francisco.
Papaloizou, J. & Pringle, J., 1978. *Mon. Not. R. astr. Soc.*, **184**, 501.
Riesz, F. & Sz.-Nagy, B., 1955. *Functional Analysis*, Frederick Ungar Publishing Co., New York.
Schutz, B. F., 1980a. *Mon. Not. R. astr. Soc.*, **190**, 7.
Schutz, B. F., 1980b. *Mon. Not. R. astr. Soc.*, **190**, 21.
Schutz, B. F., 1980c. *Phys. Rev. D15*, **22**, 249.
Schutz, B. F. & Bowen, A. M., 1983. *Mon. Not. R. astr. Soc.*, **202**, 867.
Unno, W., Osaki, Y., Ando, H. & Shibahashi, H., 1979. *Nonradial Oscillatons of Stars*, University of Tokyo Press.
Verdaguer, E., 1983. *Mon. Not. R. astr. Soc.*, **202**, 903.

Appendix: a simple test for numerical accuracy

Because our numerical method uses expansions in basis functions $\{P^m_{2l+m}\}$, truncation of the expansion at some maximum value N of l means throwing away short-wavelength information. One can always test whether this is important by increasing N and, say, looking at the change in the eigenfrequency, but this can be expensive. It turns out that there is an easy way of detecting numerical inaccuracy by looking at the eigenfunction of the mode for fixed N.

The expensive part of the numerical calculation is finding an eigenfrequency. Once the eigenfrequency is known, it is a simple matter to find the left- and right-eigenvectors for that eigenfrequency, equations (15) and (16). These are found as a series of coefficients – e.g. for $|r\rangle$ we find $\{r_i, i = 0, \ldots, N\}$ – in expansions on the basis functions:

$$|r\rangle = \sum_{j=0}^{N} r_j |b_j\rangle, \qquad \langle l| = \sum_{j=0}^{N} l_j \langle b'_j| \tag{24}$$

where in our case $|b_j\rangle$ is the basis function $P^m_{2j+m}(\eta)$ and $\langle b'_j|$ is the orthonormal conjugate basis with respect to integration over η from 0 to 1,

$$\langle b'_j| = \frac{(4j + 2m + 1)(2j)!}{2\pi(2j + 2m)!} P^m_{2j+m}(\eta). \tag{25}$$

This guarantees that

$$\langle b'_j | b_k\rangle = \delta_{jk}. \tag{26}$$

One might expect that a test of the accuracy of the mode is whether the expansions (24) converge, but it is not immediately clear what this means. Naively one might hope that r_j should get small as $j \to N$, but this depends on the normalization of $|b_j\rangle$: replacement of $|b_j\rangle$ by $N_j|b_j\rangle$ scales r_j to r_j/N_j, which can be made as small as one likes by choosing N_j appropriately. However, this rescaling replaces $\langle b'_j|$ by $\langle b'_j|/N_j$, in order to preserve orthonormality, and this in turn sends l_j into $N_j l_j$, which will do the opposite to the

'convergence' of this series. Thus, neither of the sequences $\{r_j\}$, $\{l_j\}$ alone tests the convergence of the eigenfunction expansion.

A much better test is the convergence of the product $\langle l|r\rangle$:

$$\langle l|r\rangle = \sum_{j,k} l_j r_k \langle b_j'|b_k\rangle = \sum_{j=0}^{N} l_j r_j. \tag{27}$$

What we propose is that the expansion (24) is accurate if the products $l_j r_j$ get small as $j \to N$. These products are *independent* of rescaling the basis functions. Moreover, although the overall normalization of eigenfunctions is arbitrary (i.e. if $|r\rangle$ is an eigenvector so is $\alpha|r\rangle$), the ratio of any two of these products, $(l_j r_j)/(l_k r_k)$, is independent of this normalization.

Naturally, this criterion is not perfect, for no criterion based on fixed N can supply all the information about larger N. It is possible that the 'true' eigenfunction for some mode would have $(l_j r_j)$ getting very small as j approaches, say, 15, and then getting large again as j gets near, say, 100. Our test of accuracy for $N = 15$ would then suggest more accuracy than we were entitled to assume. Fundamentally, this requires some judgment about the physical problem and the appropriateness of the basis functions $\{|b_j\rangle\}$ to the problem. If one expects on physical grounds that the sequence $|l_j r_j|$ ought to decrease roughly monotonically, for j larger than some small value, then the criterion we propose here should be reliable. For our part, we have that expectation in this problem because we known that the basis functions are the true eigenfunctions for the special case of the uniformly rotating, incompressible disc.

In Tables 5 and 6 we present a comparison of our convergence criterion with the results of increasing N. There is good correlation between the accuracy we judge on the basis of $\langle l|r\rangle$ and the size of the change in the eigenfrequency when N changes.

It can be seen in Tables 5 and 6 – and this is borne out in our calculations in general – that the r-modes with corotation points are very inaccurate, so much so that $|l_k r_k|$ shows no sign of decreasing at all even for the larger value of N. This suggests (but of course does not prove) that the exact $\langle l|r\rangle$ does not exist, i.e. that there are no proper eigenfunctions for these modes in the exact problem. This is our principal reason for believing that we are only representing the continuous spectrum here, and representing it badly. The large changes in ω_p with N only reinforce this conclusion.

Table 5. Details of the convergence test for the eigenfunctions of two modes of the disc with $\tau = 0.3181$, computed with $N = 15$. The products $l_j r_j$ are explained in the Appendix. The columns labelled A, B, C are the separate parts for the density perturbation and certain linear combinations of the velocity potentials of equations (11)–(12). The mode with $\omega_p = 0.616226$ is the $1p^-$ mode, has no corotation point, and shows good convergence. The other mode is a high-order r-mode with a corotation point, and shows little evidence of convergence.

$N = 15$		$\omega_p = 0.616226$			$\omega_p = 0.914853$	
j	$(l_j r_j)_A$	$(l_j r_j)_B$	$(l_j r_j)_C$	$(l_j r_j)_A$	$(l_j r_j)_B$	$(l_j r_j)_C$
0	2.176 (−1)	1.171 (−2)	2.289 (−2)	3.119 (−5)	4.545 (−5)	4.618 (−5)
1	5.316 (−3)	6.098 (−3)	1.476 (−2)	6.427 (−2)	6.059 (−4)	9.088 (−5)
3	4.208 (−2)	4.092 (−2)	2.863 (−3)	2.116 (−6)	8.495 (−3)	2.551 (−4)
5	4.626 (−3)	8.163 (−3)	2.452 (−3)	5.014 (−7)	3.218 (−2)	4.029 (−4)
7	5.337 (−5)	4.985 (−4)	3.424 (−4)	1.682 (−6)	6.561 (−2)	4.315 (−4)
9	1.184 (−5)	3.846 (−5)	2.795 (−5)	1.570 (−6)	8.561 (−2)	3.213 (−4)
11	1.403 (−6)	3.571 (−6)	3.760 (−6)	8.709 (−7)	7.239 (−2)	1.456 (−4)
13	2.444 (−8)	1.109 (−7)	1.228 (−7)	2.712 (−7)	3.357 (−2)	1.706 (−5)
15	2.314 (−9)	1.026 (−8)	7.434 (−9)	2.336 (−8)	2.774 (−3)	1.578 (−6)

Table 6. The same as Table 5 for $N = 30$. The $1p^-$ mode continues to converge and values of $(l_j r_j)$ for $j \lesssim 12$ are almost unchanged from $N = 15$. The r-mode shows even less tendency to converge, and its products $(l_j r_j)$ are substantially different from $N = 15$ even for $j = 0$. This corresponds to the change in ω_p: no change to six figures for $1p^-$, 0.3 per cent change for the r-mode.

$N = 30$		$\omega_p = 0.616226$			$\omega_p = 0.912005$	
j	$(l_j r_j)_A$	$(l_j r_j)_B$	$(l_j r_j)_C$	$(l_j r_j)_A$	$(l_j r_j)_B$	$(l_j r_j)_C$
0	2.176 (−1)	1.171 (−2)	2.289 (−2)	5.694 (−6)	8.098 (−6)	8.195 (−6)
1	5.361 (−3)	6.098 (−3)	1.476 (−2)	1.149 (−6)	1.048 (−4)	1.603 (−5)
3	4.208 (−2)	4.092 (−2)	2.863 (−3)	4.749 (−7)	1.523 (−3)	4.630 (−5)
5	4.626 (−3)	8.163 (−3)	2.452 (−3)	5.189 (−9)	6.141 (−3)	7.837 (−5)
7	5.327 (−5)	4.984 (−4)	3.424 (−4)	2.779 (−7)	1.380 (−2)	9.401 (−5)
9	1.181 (−5)	3.846 (−5)	2.795 (−5)	3.448 (−7)	2.087 (−2)	8.427 (−5)
11	1.395 (−6)	3.574 (−6)	3.761 (−6)	2.685 (−7)	2.242 (−2)	5.469 (−5)
13	2.310 (−8)	1.140 (−7)	1.242 (−7)	1.472 (−7)	1.653 (−2)	2.124 (−5)
15	1.064 (−9)	7.206 (−9)	4.989 (−9)	5.116 (−8)	6.811 (−3)	4.786 (−8)
16	1.860 (−10)	2.539 (−9)	1.546 (−9)	2.178 (−8)	2.755 (−3)	3.355 (−6)
20	2.322 (−13)	2.389 (−11)	7.255 (−12)	3.307 (−9)	6.073 (−3)	1.620 (−5)
25	4.612 (−17)	5.773 (−16)	7.528 (−16)	1.505 (−8)	1.987 (−2)	1.992 (−5)
30	2.497 (−19)	1.023 (−17)	8.245 (−18)	4.905 (−10)	6.128 (−4)	1.521 (−7)